

High-power arrays of quantum cascade laser master-oscillator power-amplifiers

Patrick Rauter,¹ Stefan Menzel,¹ Anish K. Goyal,² Christine A. Wang,²
Antonio Sanchez,² George Turner,² and Federico Capasso,^{1,*}

¹Harvard University, School of Engineering and Applied Sciences, 29 Oxford St., Cambridge, Massachusetts 02138, USA

²MIT Lincoln Laboratory, 244 Wood St., Lexington, Massachusetts 02420, USA
[*capasso@seas.harvard.edu](mailto:capasso@seas.harvard.edu)

Abstract: We report on multi-wavelength arrays of master-oscillator power-amplifier quantum cascade lasers operating at wavelengths between 9.2 and 9.8 μm . All elements of the high-performance array feature longitudinal (spectral) as well as transverse single-mode emission at peak powers between 2.7 and 10 W at room temperature. The performance of two arrays that are based on different seed-section designs is thoroughly studied and compared. High output power and excellent beam quality render the arrays highly suitable for stand-off spectroscopy applications.

©2013 Optical Society of America

OCIS codes: (140.5965) Semiconductor lasers, quantum cascade; (140.3280) Laser amplifiers.

References and links

1. J. Faist, F. Capasso, D. L. Sivco, C. Sirtori, A. L. Hutchinson, and A. Y. Cho, "Quantum cascade laser," *Science* **264**(5158), 553–556 (1994).
2. C. Gmachl, F. Capasso, D. L. Sivco, and A. Y. Cho, "Recent progress in quantum cascade lasers and applications," *Rep. Prog. Phys.* **64**(11), 1533–1601 (2001).
3. A. K. Goyal, M. Spencer, M. Kelly, J. Costa, M. DiLiberto, E. Meyer, and T. Jeys, "Active infrared multispectral imaging of chemicals on surfaces," *Proc. SPIE* **8018**, 80180N, 80180N-11 (2011).
4. C. A. Kendziora, R. M. Jones, R. Furstenberg, M. Papantonakis, V. Nguyen, and R. A. McGill, "Infrared photothermal imaging for standoff detection applications," *Proc. SPIE* **8373**, 83732H, 83732H-10 (2012).
5. K. Degreif, S. Rademacher, P. Dasheva, F. Fuchs, S. Hugger, F. Schnürer, and W. Schweikert, "Stand-off explosive detection on surfaces using multispectral MIR-imaging," *Proc. SPIE* **7945**, 79450P, 79450P-8 (2011).
6. For a review on external cavity QCLs see: A. Hugi, R. Maulini, and J. Faist, "External cavity quantum cascade laser," *Semicond. Sci. Technol.* **25**(8), 083001 (2010).
7. B. G. Lee, M. A. Belkin, C. Pflügl, L. Diehl, H. A. Zhang, R. M. Audet, J. MacArthur, D. P. Bour, S. W. Corzine, G. E. Höfler, and F. Capasso, "DFB quantum cascade laser arrays," *IEEE J. Quantum Electron.* **45**(5), 554–565 (2009).
8. E. Mujagic, C. Schwarzer, Y. Yao, J. Chen, C. Gmachl, and G. Strasser, "Two-dimensional broadband distributed-feedback quantum cascade laser arrays," *Appl. Phys. Lett.* **98**(14), 141101 (2011).
9. Q. Y. Lu, Y. Bai, N. Bandyopadhyay, S. Slivken, and M. Razeghi, "2.4 W room temperature continuous wave operation of distributed feedback quantum cascade lasers," *Appl. Phys. Lett.* **98**(18), 181106 (2011).
10. H. Zhang, A. Seetharaman, P. Johnson, G. Luo, and H. Q. Le, "High-gain low-noise mid-infrared quantum cascade optical preamplifier for receiver," *IEEE Photon. Technol. Lett.* **17**(1), 13–15 (2005).
11. D. F. Welch, D. Mehuys, R. Parke, R. Waarts, D. Scifres, and W. Streifer, "Coherent operation of monolithically integrated master oscillator amplifiers," *Electron. Lett.* **26**(17), 1327–1329 (1990).
12. H. Wenzel, K. Paschke, O. Brox, F. Bugge, J. Fricke, A. Ginolas, A. Knauer, P. Ressel, and G. Erbert, "10W continuous-wave monolithically integrated master-oscillator power-amplifier," *Electron. Lett.* **43**(3), 160–161 (2007).
13. M. Troccoli, C. Gmachl, F. Capasso, D. L. Sivco, and A. Y. Cho, "Mid-infrared ($\lambda \sim 7.4 \mu\text{m}$) quantum cascade laser amplifier for high power single-mode emission and improved beam quality," *Appl. Phys. Lett.* **80**(22), 4103–4105 (2002).
14. S. Menzel, L. Diehl, C. Pflügl, A. Goyal, C. Wang, A. Sanchez, G. Turner, and F. Capasso, "Quantum cascade laser master-oscillator power-amplifier with 1.5 W output power at 300 K," *Opt. Express* **19**(17), 16229–16235 (2011).
15. P. Rauter, S. Menzel, A. K. Goyal, B. Gökden, C. A. Wang, A. Sanchez, G. Turner, and F. Capasso, "Master-oscillator power-amplifier quantum cascade laser array," *Appl. Phys. Lett.* **101**(26), 261117 (2012).
16. A. Wittmann, T. Gresch, E. Gini, L. Hvozdar, N. Hoyler, M. Giovannini, and J. Faist, "High-performance bound-to-continuum quantum-cascade laser for broad-gain applications," *IEEE J. Quantum Electron.* **44**(1), 36–40 (2008).

17. C. Pflügl, W. Schrenk, S. Anders, and G. Strasser, "Spectral dynamics of distributed feedback quantum cascade lasers," *Semicond. Sci. Technol.* **19**(4), S336–S338 (2004).
18. A. Yariv and P. Yeh, *Photonics: Optical Electronics in Modern Communications*, 6th ed. (Oxford University Press, 2006), Chap. 16.
19. A. K. Goyal, M. Spencer, O. Shatrovov, B. G. Lee, L. Diehl, C. Pfluegl, A. Sanchez, and F. Capasso, "Dispersion-compensated wavelength beam combining of quantum-cascade-laser arrays," *Opt. Express* **19**(27), 26725–26732 (2011).
20. K. Utaka, S. Akiba, K. Sakai, and Y. Matsushima, " $\lambda/4$ -shifted InGaAsP/InP DFB lasers," *IEEE J. Quantum Electron.* **22**(7), 1042–1051 (1986).
21. M. Usami, S. Akiba, and K. Utaka, "Asymmetric $\lambda/4$ -shifted InGaAsP/InP DFB lasers," *IEEE J. Quantum Electron.* **23**(6), 815–821 (1987).
22. G. Morthier and P. Vankenwinkelberge, "*Handbook of distributed feedback laser diodes*" (Artech House, 1997).

1. Introduction

Recently, quantum cascade lasers (QCLs [1,2],) have seen increased use as sources for stand-off detection and spectroscopy systems in the mid-infrared [3–5]. The requirements for such systems have continued to motivate considerable research interest, aiming for the realization of single-mode high-power QCL sources with single-lobed intensity distributions in the far-field. Most of the recently demonstrated QCL-based spectroscopy systems rely on an external grating for the selection of the emission wavelength of a single external-cavity QCL [6]. As an alternative that does not require mechanical means for tuning, arrays of single-mode QCL devices allow purely electronic addressing of different wavelengths [7,8]. Single-mode operation of each array element can be achieved using distributed feedback (DFB) gratings. Despite the recent demonstration of DFB QCLs with an excellent cw output power of 2.4 W [9], single-mode DFB QCLs as array elements have so far been limited in their peak output power. This is due to the upper limit in ridge width for lateral single-mode operation. A powerful way to increase the output power of a QCL device while maintaining good beam quality is the realization of master-oscillator power-amplifiers (MOPAs). The latter are formed by a DFB seed laser monolithically integrated with an optical amplifier [10] and have been successfully implemented for both diode lasers [11,12] and QCLs [13,14]. Very recently, the authors have demonstrated an array of MOPA QCLs operating at a series of wavelengths between 9.2 and 9.8 μm with single-mode peak powers between 0.8 and 3.9 W [15]. In this work, we compare this first-generation MOPA array (called Array 1 in the following) to an array of MOPA QCLs featuring a DFB grating of a simplified design that will be called Array 2. A thorough experimental characterization of both arrays allows the comparison between the two design strategies, showing that a simple DFB grating approach proves superior to a counterpart based on a quarter-wave-shifted (QWS) DFB section in terms of single-mode output power. The MOPA array presented in this work (Array 2) features single-mode peak powers between 2.7 W and 10 W and excellent beam quality.

2. Material and fabrication

The material used for both Array 1 and Array 2 is a GaInAs/AlInAs broadband bound-to-continuum heterostructure [16] grown lattice-matched on a conducting InP substrate by organometallic vapor phase epitaxy (OMVPE). A 3.5- μm -thick, highly silicon-doped InP layer ($n = 1 \times 10^{17} \text{cm}^{-3}$) is followed by a 0.52- μm -thick layer of GaInAs ($n = 3 \times 10^{16} \text{cm}^{-3}$) and the active region composed of 35 periods of the following layer sequence (AlInAs barriers bold, GaInAs wells Roman, thickness in nm, underlined layers doped to $n = 1.5 \times 10^{17} \text{cm}^{-3}$): **4.4/1.7/0.9/5.3/1.1/5.2/1.2/4.7/1.3/4.2/1.5/3.9/1.6/3.4/1.8/3.1/2.1/2.8/2.5/2.7/3.2/2.7/3.6/2.5**. Following the growth of an additional injector sequence and 520 nm of GaInAs ($n = 3 \times 10^{16} \text{cm}^{-3}$), the structure is completed by the upper waveguide cladding formed by

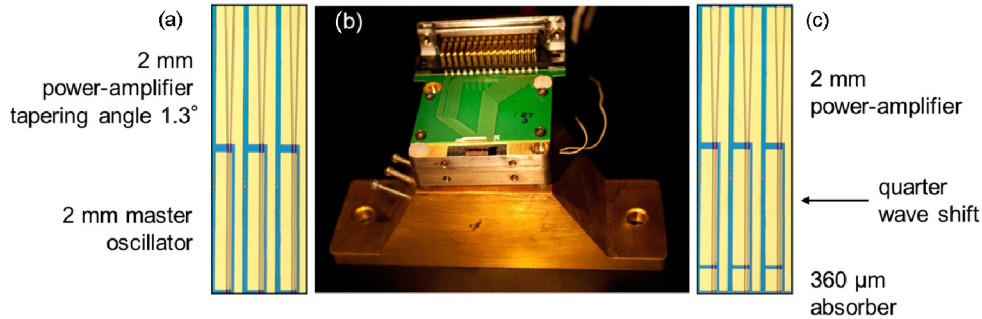


Fig. 1. Layout and packaging. a) The elements of Array 2 comprise a 2-mm-long DFB section and an equally long tapered power-amplifier with a taper angle of 1.3° . b) Packaged array, allowing individual electronic addressing of both device sections for all of the array elements. c) Top view of three elements of Array 1, for which a quarter-wave shift was included in the DFB grating at the indicated position. Note that $360\ \mu\text{m}$ of the 2-mm-long DFB section are left unpumped.

$3.5\ \mu\text{m}$ of InP ($n = 1 \times 10^{17}\text{cm}^{-3}$), the top contact layer composed of $0.5\ \mu\text{m}$ of InP ($n = 5 \times 10^{18}\text{cm}^{-3}$), and $20\ \text{nm}$ of GaInAs ($n = 1.8 \times 10^{19}\text{cm}^{-3}$).

An array of sixteen QCL MOPA devices was fabricated. Each MOPA comprises two sections, a narrow DFB ridge acting as a master-oscillator (MO), and a tapered power-amplifier (PA). While the geometric layout and dimensions of both arrays described in this work are identical to that in reference [15], the two arrays differ in their DFB grating design. Array 2 features a conventional first-order Bragg grating, while a QWS was introduced in the grating of Array 1. To fabricate DFB gratings, the top InP cladding layer was first removed by wet etching in a HCl:H₂O (1:1) solution. The grating was then defined by electron-beam lithography and subsequent ion-etching into the exposed 520-nm-thick GaInAs layer with an etch depth of 250 nm. The DFB grating period was varied between $1.55\ \mu\text{m}$ (device 1) and $1.44\ \mu\text{m}$ (device 16) in order to achieve a different emission wavelength for each array element. After the DFB gratings were etched, the InP cladding and top-contact layer sequence were regrown using OMVPE. The device geometry was defined by reactive ion-etching of double trenches where $13\ \mu\text{m}$ wide DFB ridges and an amplifier tapering half-angle of 1.3° were realized. A Ti/Au metallization was applied as a ridge top contact and 450-nm-thick SiN provides electrical insulation.

The MO and PA sections were separated electrically by a $100\text{-}\mu\text{m}$ -wide gap in the gold metallization. The MO and PA sections were each 2-mm-long and the output facet was $110\text{-}\mu\text{m}$ -wide. Anti-reflection (AR) coatings were applied to the latter allowing for strong optical amplification in single-pass travelling-wave configuration. The AR coating is composed of 842-nm-thick ZnS (refractive index of 2.2) and 1280-nm-thick YF₃ (refractive index of 1.415). Adhesion between the layers is provided by 30 nm of Y₂O₃. The substrate was maintained at 175°C during e-beam evaporation of the coating. During the deposition of YF₃, argon ion-assisted-deposition was used to increase the density of the film and to improve its mechanical stability under thermal cycling. The AR coating applied to the front facet of the PA increased the self-lasing threshold of the tapered section from about 4.2 A to 6.6 A in the case of an unpumped MO. Figures 1(a) and 1(c) show a top view of three elements of Array 2 and Array 1, respectively. The top metallization of the PA is extended alongside the MO section of the devices in order to enable clean bonding and packaging. The array chip was mounted epilayer up on a heat sink and packaged as seen in Fig. 1(b).

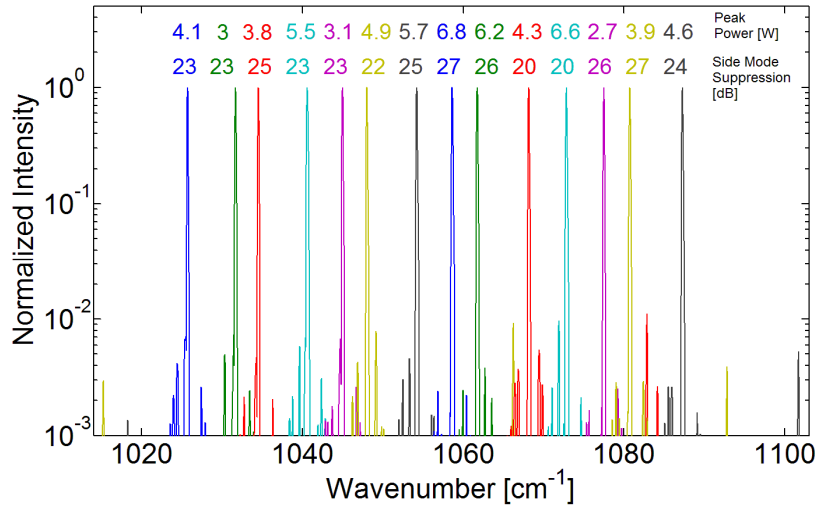


Fig. 2. Emission spectra of the array elements. For each device of the MOPA array, a logarithmic plot of the spectrum at maximum single-mode peak power for PA currents below the self-lasing threshold is shown together with the respective power and side-mode suppression ratio. The spectra have been normalized to their maximum, where the leftmost and rightmost curves represent device 2 and 15, respectively. The measurements were performed at room temperature and a duty cycle of 0.025%. Note that for device 9 single-mode operation at peak powers up to 10 W can be achieved for amplifier currents *above* the self-lasing threshold, as discussed in the text.

3. Experimental results for array 2

Each element of Array 2 was characterized under pulsed operation (10 kHz repetition rate, 25 ns MO pulse length, 100 ns PA pulse length) at a heat sink temperature of 18°C. A short MO pulse was employed to limit spectral broadening due to self-heating of the device. The difference in the pulse lengths for the MO and PA is due to limitations of the pulse generator used for driving the PA. The length of the output radiation bursts is determined by the MO pulse length as the amplifier is driven below its self-lasing threshold. This gives a duty cycle of 0.025% for all of the experiments in this work except when explicitly mentioned otherwise.

A systematic characterization procedure determined the maximum achievable peak output power of each MOPA element while maintaining a side-mode suppression ratio (SMSR) of at least 20 dB. This was accomplished by monitoring the output spectra of the individual devices using a Fourier-transform infrared spectrometer while the currents through the MO and PA were successively increased.

Figure 2 shows a logarithmic plot of these spectra at the maximum single-mode power for all of the operating devices along with the respective peak power (measured using a calibrated bolometer) and the SMSR. Two of the 16 array elements suffered from fabrication defects: Device 1 did not show lasing due to a short, while the PA section of device 16 exhibited an unacceptably low self-lasing threshold of 4.5 A likely related to a defective AR coating. Whenever the self-lasing threshold of the PA is mentioned, this refers to the respective value for an unpumped MO. The spectra in Fig. 2 show that each array element operates at a different wavelength between 9.2 μm (device 15) and 9.75 μm (device 2). All of the devices are capable of single-mode operation at peak powers in excess of 2.7 W, with ten MOPAs featuring single-mode peak powers at or above 3.9 W. For PA currents below the self-lasing threshold, device 9 reaches a single-mode peak power of 6.8 W. As will be discussed later in this section, device 9 is capable of single-mode operation at amplifier

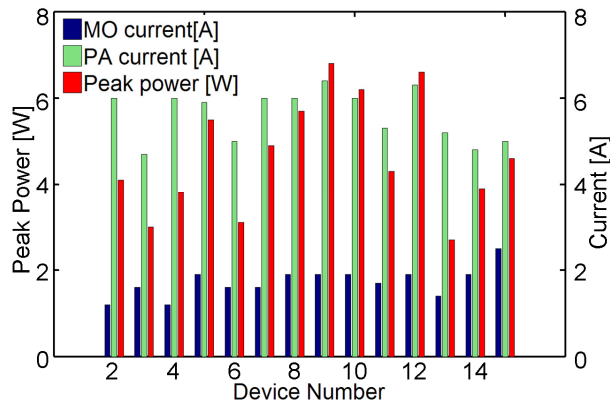


Fig. 3. Optimum driving conditions: The plot presents the values for master-oscillator (blue bars) and power-amplifier peak currents (green bars), at which the spectra in Fig. 2 have been acquired, together with the corresponding peak power values (red bars).

currents beyond the self-lasing threshold. Figure 2 indicates that each of the array elements exhibits an excellent SMSR ratio between 20 and 27 dB. Also, it is seen that the emission wavenumbers of the array elements are not equidistant. This is due to lasing of some of the devices at the lower-frequency edge of the photonic bandgap, while a majority of elements lase at the higher-frequency edge state. Lasing at the higher-frequency edge is more likely due to its lower waveguide loss, but lasing at the lower-frequency edge state of the photonic bandgap occurs under certain conditions due to the influence of the device facets [7].

Figure 3 presents the driving parameters at which the spectra shown in Fig. 2 were acquired along with the corresponding peak powers. The highest single-mode peak powers are reached by elements which allow simultaneous driving of the MO close to rollover (around 2 A) and of the PA close to its self-lasing threshold (devices 5, 8, 9, 10 and 12). Increasing the PA or MO current beyond the values in Fig. 3 leads to unwanted multi-mode behavior of the devices, where the absolute upper limit for driving the MO is given by the rollover current. Representative multimode spectra are shown in Fig. 4 for device 5 and device 13. For the latter, the highest output power for single-mode operation is achieved by driving the MO and PA at 1.4 A and 5.2 A, respectively. Both increasing the MO current to 1.6 A (Fig. 4(a)) and raising the PA current to 5.4 A (Fig. 4(b)) results in multi-mode behavior, where the origin of the additional modes is discussed in the following.

For all of the array elements, an increase of the *PA current* beyond the values given in Fig. 3 results in a degradation of the SMSR below 20 dB due to the appearance of a group of additional modes (with the exception of device 9, as discussed later on). These groups of additional modes can be identified as Fabry-Perot (FP) modes and typically appear at two different spectral positions. For devices 4, 11, 13, 14 and 15, the FP modes appear in the spectral region around 1010 cm^{-1} and exhibit a free spectral range of 0.37 cm^{-1} (see Fig. 4(b)), suggesting a cavity length of 4 mm which is equivalent to the total device length. The cavity for these modes is thus formed by the two device facets. Devices 2, 3, 5, 6, 7, 8, 10 and 12, on the other hand, exhibit lasing at additional modes that are in, and close to, the photonic bandgap with a free spectral range of 0.8 cm^{-1} (see Fig. 4(c)). These modes originate from self-lasing of the tapered PA section where the DFB section acts as a distributed Bragg reflector forming a 2-mm-long cavity together with the PA front facet. Figure 4(c) shows a representative spectrum for device 5 at high PA currents, where the PA exhibits self-lasing at FP modes within the photonic bandgap (labeled 2 and 3) in addition to the high-frequency

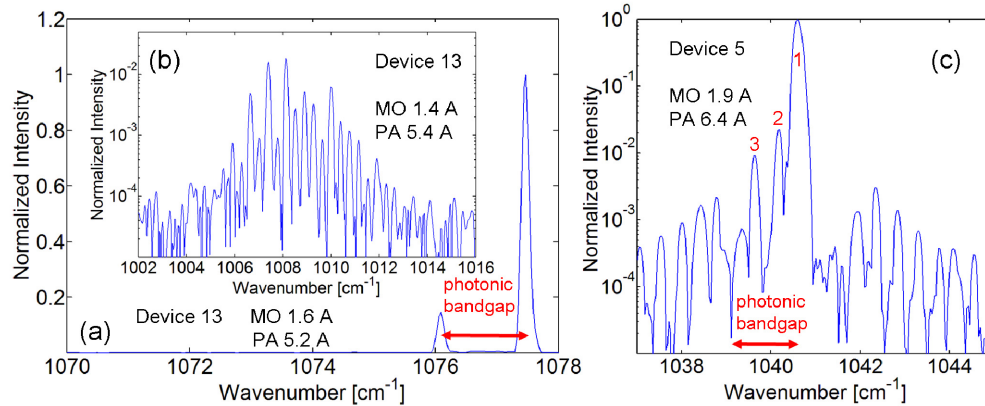


Fig. 4. Additional modes at high driving currents. The plot shows three different scenarios compromising the single-mode operation of the array elements for driving current values in excess of those in Fig. 3. The spectra are normalized to the maximum intensity of the dominant DFB mode. a) An increase of the master-oscillator current of device 13 beyond 1.4 A results in lasing at both the high- and low-frequency DFB mode. b) For the same array element, an increase in the power-amplifier current beyond 5.2 A enables lasing at Fabry-Perot modes of the cavity formed by the MO and PA sections. Note that the additional modes are located at low frequencies and the DFB mode at 1077.5 cm^{-1} is not shown in the plot. c) When increasing the PA current of device 5 in excess of 6.2 A, Fabry-Perot modes (labeled 2 and 3) appear within the indicated photonic bandgap in addition to the high-frequency DFB mode (labeled 1).

DFB mode (labeled 1) seeded by the MO. In future devices, higher single-mode power can be achieved by decreasing the residual reflectivity of the AR coated facet and thus further suppressing self-lasing of the PA.

Seven array elements can be driven at MO currents close to rollover for single mode operation. In contrast, devices 2, 3, 4, 6, 7, 11 and 13 show multimode emission when increasing the *MO current* beyond the values given in Fig. 3 and approaching the rollover current of the seed section. The DFB sections of devices 3, 4 and 13 exhibit lasing on both the low- and high-frequency DFB modes at high driving currents as a result of the influence of the back facet and/or the front facet. A representative spectrum is shown in Fig. 4(a) (device 13) from which one determines a photonic bandgap of 1.5 cm^{-1} . For devices 2, 6, 7 and 11, the single mode operation of the DFB section at high MO currents is compromised either by side-modes close to the photonic bandgap, or by modes more than 10 cm^{-1} away from the Bragg wavenumber of the DFB grating.

The considerable difference in the maximum single-mode output power between the individual array elements is thus related to the influence of the two device facets on the MOPA performance. The negative influence of the device facets on the reliable single-mode operation of DFB lasers without AR coating is well-known for diode lasers and has been extensively studied in [7] for an array of DFB QCLs. For a MOPA with a residual front-facet reflectivity, the complexity of the system increases as it involves coupled cavities. For next-generation MOPA arrays, an improvement in the AR coating performance and the application of an AR coating on the back facet can lead to a greater uniformity in maximum single-mode power at each of the targeted array wavelengths.

For all of the array elements except device 9, an increase in the amplifier current beyond the values given in Fig. 3 leads to multimode emission due to self-lasing of the amplifier. The PA current given for device 9 in Fig. 3 is slightly below the self-lasing

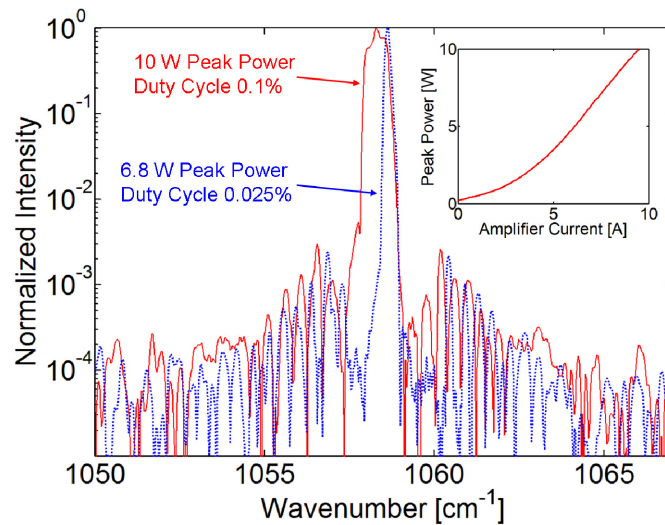


Fig. 5. Room-temperature performance of device 9 for high amplifier currents beyond the self-lasing threshold of the amplifier. The inset shows the light/amplifier-current characteristics acquired by driving both the master-oscillator and power-amplifier section of device 9 with 100-ns-long pulses. The red curve shows the normalized spectrum acquired at a MO current of 2.3 A and a PA current of 9.5 A, giving a peak output power of 10 W. The difference in width between the blue curve representing the emission spectrum of device 9 for a lower duty cycle of 0.025% and the spectrum shown in red is due to self-heating and exclusively relates to the difference in driving pulse length of the MO.

threshold, and thus is the upper limit for a straight-forward operation of the PA as a single-pass amplifier. However, the single-mode operation of device 9 persists even for PA currents far beyond the self-lasing threshold of the device, up to the maximum driving current accessible by the pulse generator. A characterization of device 9 for PA currents above self-lasing threshold requires driving of both sections with equally long pulses. As the shortest pulse length delivered by the pulse generator powering the PA section is 100 ns, both sections were driven by 100-ns-long pulses when acquiring the data presented in Fig. 5. The inset shows a plot of the light/amplifier-current characteristics measured for a MO current of 2.3 A where a peak power value of 10 W is reached for a PA current of 9.5 A. The maximum power was limited by the pulse generator and not by the loss of single-mode operation. The red curve in Fig. 5 presents the spectrum acquired for a MO/PA current of 2.3/9.5 A, and demonstrates single-mode operation with a SMSR of 24 dB at 10 W peak power. Note that the emission spectrum at 10 W is significantly broadened as compared to that presented for 6.8 W. The difference in spectral linewidth between the two curves is due to self-heating during the driving pulses [17]. While the FWHM is less than 0.2 cm^{-1} for a MO pulse length of 25 ns, it increases to 0.7 cm^{-1} for a 100-ns-long pulse. This behavior is not related to the output power and is observed over the whole range of PA currents.

As the tapered section of a MOPA acts as an optical amplifier, the dependence of the output power on the PA current differs from the linear light-current (LI) characteristics typical for laser operation. This is demonstrated by Fig. 6 which presents the light/amplifier-current characteristics for device 9 at a series of MO currents from threshold to rollover (25-ns-long MO pulse width, 0.025% duty cycle). At low MO and PA currents, the output power exhibits the exponential dependence typical for single-pass travelling-wave amplifiers. The output power P_{out} of the device follows $P_{\text{out}} = P_{\text{in}} \cdot \exp[-\alpha_w + g \cdot \Gamma \cdot (j - j_{\text{trans}})] \cdot d] = P_0 \cdot \exp[g \cdot \Gamma \cdot j \cdot d]$, where P_{in} is the input power from the DFB section, α_w are the waveguide losses, d is the

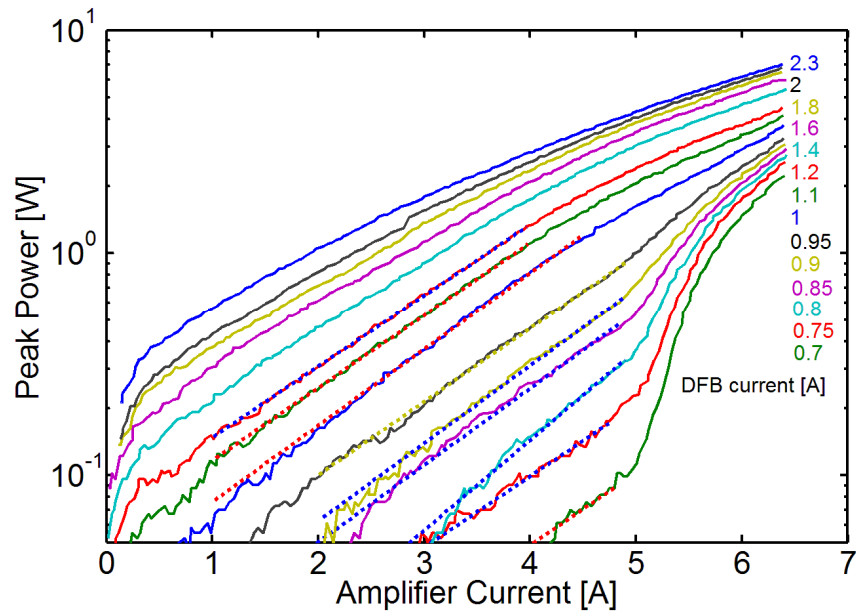


Fig. 6. Light/amplifier-current characteristics of device 9 for different master-oscillator currents. Note the exponential dependence for low MO and amplifier currents, typical of travelling-wave single-pass amplifiers. An exponential fit of the characteristics in this regime (shown by the dotted curves) allows the extraction of the modal gain coefficient of the amplifier. Note the deviation from the exponential behavior due to gain saturation at high MO and amplifier currents.

amplifier length, j the PA current density, j_{trans} the transparency current density of the PA and $g \cdot \Gamma$ the modal gain coefficient. An exponential fit of the low-current data in Fig. 6 up to a DFB current of 1.2 A allows the extraction of the modal gain coefficient. A value of $g \cdot \Gamma = 4.7$ cm/kA is obtained when averaging over the respective fit parameters of the individual curves. Analogously, the modal gain coefficients for all array elements are extracted from the unsaturated characteristics measured at a DFB current of 1.1 A (not shown), where values between 4.3 and 5.2 cm/kA are found. The array average of 4.8 cm/kA for the gain coefficient is consistent with the value reported for Array 1 in [15]. The flattening of the characteristics for high MO and PA currents is well known and is caused by gain saturation.

In the regime of very low MO currents, the seeded mode is too weak to induce significant gain competition and efficiently suppress self-lasing of the amplifier section. The threshold for self-lasing of the PA on modes of the cavity formed either by the PA or both the MO and PA is influenced significantly by feedback from the MO and thus by losses or gain in this section. Compared to the case of an unpumped MO section, the losses determining the PA self-lasing threshold are reduced significantly when pumping the MO. At relatively low MO currents slightly above threshold, self-lasing of the PA thus sets already in around 5.2 A and dominates the LI curve, resulting in the linear characteristics expected for conventional lasers. This interpretation of the LI-curves for MO currents below 1 A is confirmed by the corresponding spectra presented for device 9 in Fig. 7. As seen in the inset of Fig. 7, for a high MO current the tapered section acts as an amplifier at a PA current of 6 A, resulting in single-mode emission of the MOPA. However, in case of very low MO currents, self-lasing of the the PA is observed for the same amplifier current of 6 A, with FP modes appearing around 1000 cm^{-1} (labeled 3 in Fig. 7). The additional mode (labeled 2) close to the high-frequency

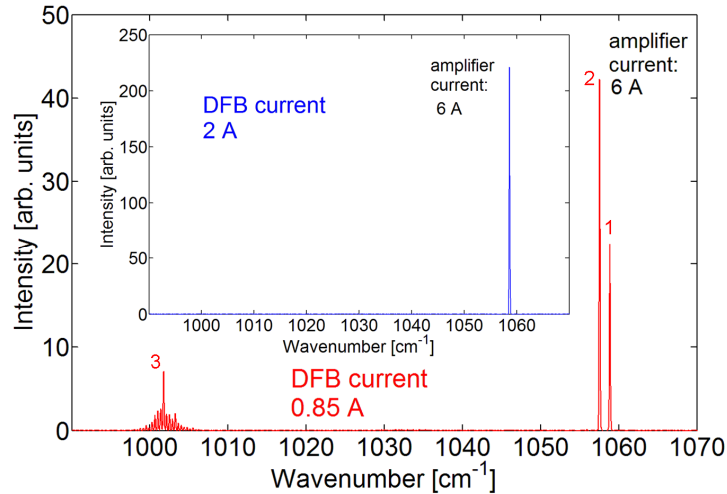


Fig. 7. Self-lasing of the power-amplifier at very low seed intensities for device 9. In addition to the high-frequency DFB mode (labeled 1), the red curve shows the appearance of FP modes of the amplifier section (labeled 3) at a low DFB current of 0.85 A and a high amplifier current of 6 A. The mode close to the lower edge of the photonic bandgap (labeled 2) is either the low-frequency DFB mode of the MO, or a self-lasing FP mode of the PA. At low MO currents, the intensity of the seeded mode is too weak to effectively suppress self-lasing of the PA section by gain competition. In contrast, for high DFB currents no PA self-lasing on additional modes is observed up to high amplifier currents, as shown in the inset.

DFB mode (1) could not be clearly identified, and either originates from self-lasing of the PA within the photonic bandgap close to its edge, or from lasing of the MO at the low-frequency DFB mode.

The clear signs of gain saturation seen in Fig. 6 imply that the performance of future MOPA arrays can be pushed towards higher output power by increasing the tapering angle of the PA section. For larger tapering angles, the mode seeded by the DFB section spreads adiabatically over a larger device cross-section while travelling through the amplifier, thus shifting the onset for gain saturation to higher powers. It is worth noting that an increase in the tapering angle for a given device length *only* increases the output power if the amplifier suffers from gain saturation.

Figure 8 presents the far-field intensity distribution in the chip plane for each element of Array 2 which was measured using a HgCdTe detector mounted on a rotating arm at a distance of 18 cm from the device facets. During the experiment, the devices were driven under conditions for maximum single-mode power as given in Fig. 3. For all devices, a single-lobed far-field distribution is observed with only minor contributions by higher-order lateral modes for some array elements (6, 7, 8, 10 and 11). A single-lobed far-field distribution of Gaussian shape indicates the seeding of a single TM_{00} mode as well as the adiabatic spreading of the seeded mode during amplification. Figure 9(a) compares the clean far-field distribution of device 2 and those of devices 8 and 11 which show higher-order-contributions. The dotted red curve represents a Gaussian fit of the far-field intensity distribution of device 2. As evident from this plot, the higher-order contributions observed for some of the devices are minor. All devices exhibit an in-plane far-field distribution with a FWHM between 6.8° and 8.2° with an average FWHM of 7.8° . These FWHM values compare well to the theoretical estimate of $\theta = 5.2^\circ$ for the diffraction-limited in-plane divergence angle. This theoretical estimate was obtained by approximating the sinusoid in-plane field distribution of the amplifier mode at the facet by a Gaussian with an equivalent intensity standard deviation (Gaussian spot size of $w_0 = 39.6 \mu\text{m}$) and using $\theta = 180^\circ/\pi \cdot (2 \cdot \ln 2)^{0.5} \cdot \lambda / (\pi \cdot w_0)$ where λ is the

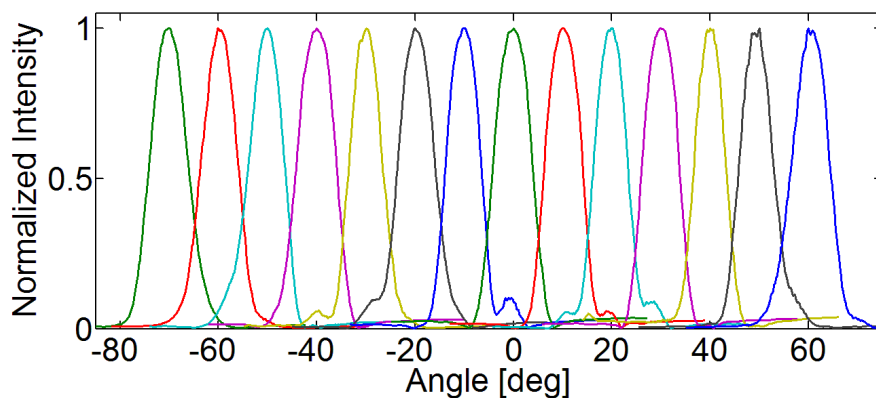


Fig. 8. Angular in-plane distribution of the far-field intensity for all devices. The leftmost curve represents device 2 and the rightmost device 15. The devices were operated at maximum single-mode power, at the driving parameters given in Fig. 3, and thus correspond to the spectra shown in Fig. 2. The plots have been offset horizontally for clarity.

average emission wavelength [18]. The green curve in Fig. 9 shows the far-field distribution of device 9 under driving conditions for 10 W peak power. While the intensity distribution at 10 W is slightly broader than that of the same device for 6.8 W, with a FWHM of 9° as compared to 8.2° , an excellent beam quality is maintained even at 10 W peak power. The single-lobed far-field plots in Fig. 8 demonstrate, together with the corresponding spectra shown in Fig. 2, that each element of Array 2 is capable of high-power operation while remaining single-mode in both the longitudinal and transverse dimensions.

4. Comparison between Arrays 1 and 2

As mentioned above, the array demonstrated in this work (Array 2) differs from that reported in reference [15] (Array 1) in its DFB section design. For Array 1, a QWS was introduced in the DFB grating of each MO [15] with the motivation of eliminating the uncertainty in the actual lasing wavelength. For applications requiring beam combining of the output of the array elements using a diffraction grating, an equidistant frequency spacing of the individual devices is essential [19]. In work with diode lasers, DFB gratings with QWS have been investigated [20] for the same reason. The introduction of a QWS creates a defect state in the center of the photonic bandgap where the defect-state mode experiences significantly lower losses than the band-edge modes due to spatial confinement and the attendant less efficient out-coupling of its power.

For Array 1, in addition to the QWS, an absorbing section was included next to the MO back facet with the purpose of suppressing the influence of the back facet on the mode selection. Figure 1(c) shows this absorber section which is formed by an electrically separated and unpumped 360- μm -long segment. While Array 1 exhibits single-mode peak powers between 0.8 and 3.9 W with an excellent beam quality [15], the QWS did not result in the anticipated lasing at equally spaced frequencies. This is attributed to a number of parameters such as the coupling coefficient of the grating, the exact position and precise width of the defect, as well as the residual influence of the device facets [21].

Figure 10 compares the single-mode spectra and corresponding peak power of each element of Array 1 (in blue) to those measured for Array 2 (in red). For Array 2, the spacing between the emission lines of two neighboring array elements is either given by about $\Delta\nu$, $\Delta\nu + \Delta\nu'$ or $\Delta\nu - \Delta\nu'$, where $\Delta\nu = 4.6 \text{ cm}^{-1}$ is the spacing between the individual Bragg wavenumbers, and $\Delta\nu' = 1.5 \text{ cm}^{-1}$ is the width of the photonic bandgap. Based on the observed spacing between the spectra, a clear distinction between lasing on the *lower* and *upper* edge

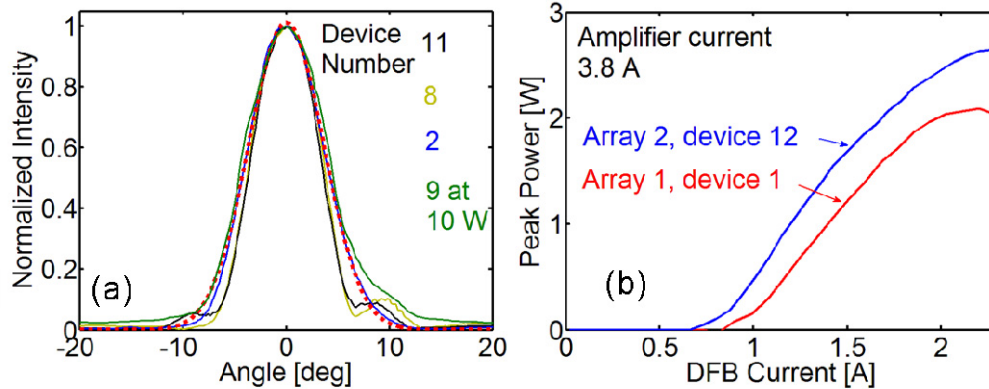


Fig. 9. Angular in-plane distribution of the far-field intensity of Array 2 and typical light/DFB-current characteristics for Array 1 and 2 at constant amplifier current. a) The black and yellow curves highlight the minor contributions by higher-order lateral modes for two representative devices (11 and 8, respectively), where such contributions are observed for five of the array elements. The far-field of device 2, shown by the blue curve, is free of contributions by higher-order modes, as are the intensity distributions of nine devices at their maximum single-mode peak power. The red, dotted curve presents a Gaussian fitted to the blue curve. The angular intensity distribution of device 9 is shown by the green curve for a DFB/amplifier current of 2.3/9.5 A and at 10 W peak power, demonstrating the preservation of its excellent beam quality even at high output powers. b) On average, the elements of Array 1 exhibit a slightly lower slope efficiency than those of Array 2. Note that the slope of the presented curves is increased compared to the actual slope efficiency of the DFB section by the amplification factor associated with the power-amplifier.

state of the photonic bandgap can be made. The letters L/U next to the peak power values indicate lasing on the lower/upper edge state, respectively, and the thin red diagonal lines connect the peak positions of the spectra on the same side of the bandgap. Note that the bandgap position slightly deviates from the equidistant case. From the observed width of the photonic bandgap, a κL of about 3 is gained from $\kappa = \pi n_0 \Delta v$, where κ is the coupling coefficient, L is the grating length and n_0 the average refractive index of the ridge [22]. Nine elements of Array 2 lase on the upper, and five on the lower edge state of the photonic bandgap. This is consistent with the ratio of 75:25 predicted in [7] for a DFB QCL with a κL of 4.6 and with AR coating on one facet. For Array 1, the determination of the emission frequency with respect to the Bragg wavenumber is far more difficult than for Array 2, as there are now three different and relatively closely spaced potential wavenumbers for lasing: The lower and upper edges of the photonic bandgap, and the defect state in the center of the bandgap formed by the QWS. Thus, a clear identification of the three different positions relies on a reference for the bandgap position and therefore on a comparison to Array 2. The lasing wavelengths of Array 1 relative to the photonic bandgap are indicated by the capital blue letters next to the respective power values, where “C” marks lasing on the defect state in the center of the bandgap. As seen from the plot, seven elements of Array 1 lase on the central defect state, five on the higher-frequency state and three on the lower-frequency state of the photonic bandgap. The blue diagonal line in Fig. 10 connects the emission wavenumbers of the array elements lasing at the center of the photonic bandgap.

Array 1 and 2 exhibit a striking difference in the achieved single-mode peak power, with maximum values between 0.8 and 3.9 W for Array 1 and values between 2.7 W and 10 W for Array 2. As the PA sections of the two devices are equivalent in every aspect, the difference in the maximum accessible single-mode power is directly related to the difference in the design of the MO section. Light/DFB-current characteristics recorded for both arrays at a constant PA current of 3.8 A indicate, that the power seeded by the DFB sections is

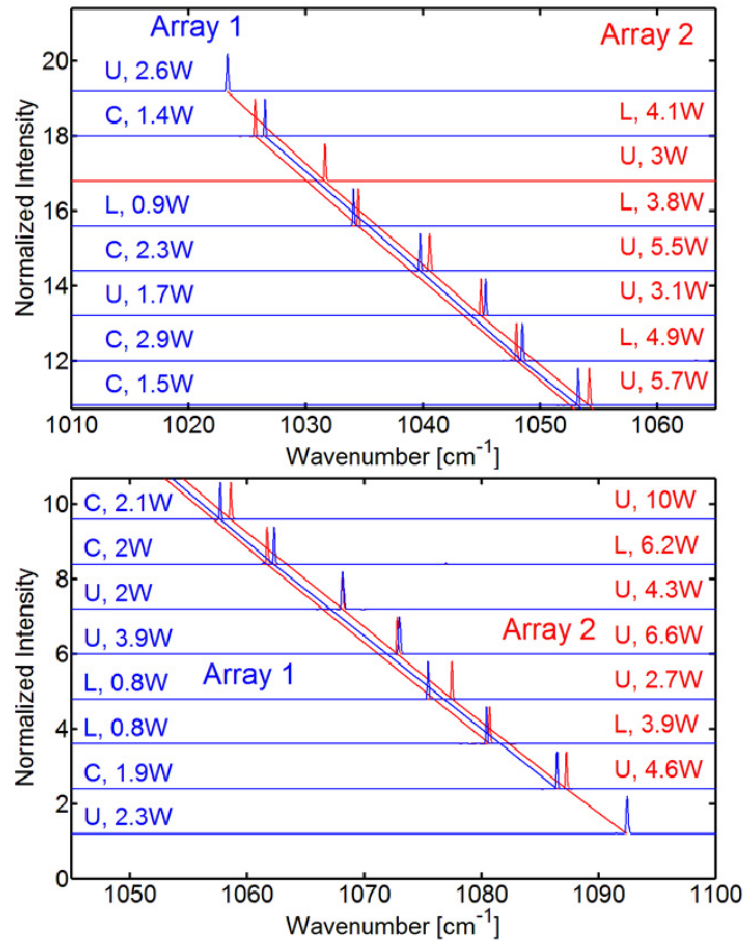


Fig. 10. Spectral comparison between Array 1 (with quarter-wave-shift) and Array 2 (without QWS). The plot shows the single-mode spectra for each array element of Array 1 and 2 in blue and red, respectively. The power values given in the same color compare the maximum peak power available for single-mode operation for the individual devices. Lasing on the upper and lower edge of the photonic bandgap is denoted by U (right diagonal red line) and L (left red line), respectively. For Array 1, lasing on the defect state in the center of the photonic bandgap is denoted by C (blue diagonal line).

comparable for both arrays at equivalent driving conditions. Figure 9(b) shows the measured LI curve for a representative device from each array. For Array 1, the threshold currents for the MOs range between 0.8 and 1 A (except for device 3 which suffers from high leakage current) with an average of 0.9 A. At low MO currents, the average slope efficiency (which includes the amplification factor of the PA) is 2.4 W/A. For Array 2, the average threshold current of the MO sections is comparable to that of Array 1, with values between 0.7 and 1.1 A, and an average of 0.83 A. The average slope efficiency for Array 2 is 2.6 W/A. As the amplification factor can be assumed equal for both arrays at the same PA current, the DFB sections of Array 2 exhibit slightly higher slope efficiencies than those of Array 1. At an amplifier current of 3.8 A and at the rollover current of the MO, the difference in seeded power due to the different MO design results in an average of about 15% lower output power for Array 1. The lower seeded power is expected for MO section with a QWS, as compared to an equivalent MO without a QWS, due to the confinement of the mode to the defect state in

the QWS DFB. This small difference in seeded power, however, does not explain the large difference in maximum single-mode output power between the two arrays.

The large power difference is thus primarily related to the stability of single-mode operation. As evident when comparing the driving parameters for optimum single-mode operation of Array 2 in Fig. 3 to those of Array 1 as given in [15], the accessible DFB current range is comparable for both arrays, with seven MO sections capable of single-mode emission close to rollover for both arrays. On the other hand, the accessible amplifier current range for single-mode operation of Array 1 is significantly narrower than that of Array 2. The operation of Array 1 is typically compromised by the appearance of additional modes at significantly lower amplifier currents than that of Array 2, and is therefore far more sensitive to radiation coupled back from the front facet of the PA.

An explanation for the multimode operation of Array 1 at relatively low PA currents can be found when analyzing the spectral position of the additional modes. The single-mode operation of Array 2 is compromised at high PA currents due to self-lasing of the amplifier, as discussed in the previous section. In contrast, for eleven array elements of Array 1 the additional modes appearing at higher PA currents can be associated with simultaneous lasing at the QWS defect state and one edge state of the photonic bandgap. This implies that for most elements of Array 1 single-mode operation is already compromised at PA currents far below the self-lasing threshold due to multi-mode seeding by the MO section itself. For diode lasers, the problem of multi-mode operation for QWS DFB devices has been extensively studied and a reduction of the reflectivity of both device facets below 2% is suggested in [20] for guaranteeing reliable single-mode operation. For a MOPA, the prediction of the influence of the front facet is far more complex due to the tapered device geometry and the coupled-cavity configuration. Thus, improving the *stability of single-mode operation* of the QWS MO requires either a decrease in the residual reflectivity of the PA front facet, an additional AR coating applied to the MO facet, or a comprehensive re-design of the position of the QWS by considering both MOPA sections.

5. Summary

In conclusion, we have demonstrated a high-power QCL MOPA array operating at fourteen different wavelengths between 9.2 and 9.8 μm . Each element is capable of single-mode operation (SMSR > 20 dB) at peak power values between 2.7 W and 10 W. The individual devices exhibit single-lobed far-field characteristics with an average FWHM angle of the narrow in-plane intensity distribution of 7.7°. With its high peak output power of several Watts per element (10 out of 14 devices were capable of peak powers between 3.9 and 10 W), clean single-mode spectra and excellent beam quality up to these high power values, the demonstrated QCL MOPA array is highly suitable as a source for stand-off detection and spectroscopy systems for a broad variety of applications from hazard detection to environmental studies.

Acknowledgments

The authors gratefully acknowledge the expert assistance of Jon Wilson for applying anti-reflection facet coatings and of Leo Missaggia for packaging devices. The authors acknowledge the Center for Nanoscale Systems (CNS) at Harvard University. Harvard CNS is a member of the National Nanotechnology Infrastructure Network (NNIN). This project received support from the Defense Threat Reduction Agency-Joint Science and Technology Office for Chemical and Biological Defense (Grant no. HDTRA1-10-1-0031-DOD). P. Rauter acknowledges support from the Austrian Science Fund (FWF): J 3092-N19. The Lincoln Laboratory portion of this work was sponsored by the Office of the Assistant Secretary of Defense for Research and Engineering under Air Force contract No. FA8721-05-C-0002. The opinions, interpretations, conclusions, and recommendations are those of the authors and are not necessarily endorsed by the United States Government.